nanomaterials

MDPI

Article

Solution-Processed PEDOT:PSS/MoS_2 Nanocomposites as Efficient Hole-Transporting Layers for Organic Solar Cells

Madeshwaran Sekkarapatti Ramasamy, Ka Yeon Ryu, Ju Won Lim, Asia Bibi, Hannah Kwon, Ji-Eun Lee, Dong Ha Kim * and Kyungkon Kim *

Deprtment of Chemistry and Nanoscience, Ewha Womans University, 52 Ewhayeodae-gil, Seodaemun-gu, Seoul 03760, Korea

* Correspondence: dhkim@ewha.ac.kr (D.H.K.); kimkk@ewha.ac.kr (K.K.)

Received: 6 July 2019; Accepted: 11 September 2019; Published: 16 September 2019

Abstract: An efficient hole-transporting layer (HTL) based on functionalized two-dimensional (2D) MoS_2-poly(3,4-ethylenedioxythiophene):poly(styrenesulfonate) (PEDOT:PSS) composites has been developed for use in organic solar cells (OSCs). Few-layer, oleylamine-functionalized MoS_2 ($FMoS_2$) nanosheets were prepared via a simple and cost-effective solution-phase exfoliation method; then, they were blended into PEDOT:PSS, a conducting conjugated polymer, and the resulting hybrid film (PEDOT:PSS/$FMoS_2$) was tested as an HTL for poly(3-hexylthiophene):[6,6]-phenyl-C_{61}-butyric acid methyl ester (P3HT:PCBM) OSCs. The devices using this hybrid film HTL showed power conversion efficiencies up to 3.74%, which is 15.08% higher than that of the reference ones having PEDOT:PSS as HTL. Atomic force microscopy and contact angle measurements confirmed the compatibility of the PEDOT:PSS/$FMoS_2$ surface for active layer deposition on it. The electrical impedance spectroscopy analysis revealed that their use minimized the charge-transfer resistance of the OSCs, consequently improving their performance compared with the reference cells. Thus, the proposed fabrication of such HTLs incorporating 2D nanomaterials could be further expanded as a universal protocol for various high-performance optoelectronic devices.

Keywords: organic solar cells; MoS_2; hole-transporting layer; oleylamine

1. Introduction

Organic solar cells (OSCs) have many striking properties such as flexibility, solution processability, light weight, and simple manufacturing, especially if compared with their inorganic counterparts. To enhance their performance, numerous strategies have been proposed, including novel photoactive materials, morphology control, interfacial engineering, plasmonic nanoparticles incorporation, and alternative buffer layers and electrodes [1–6]. Their power conversion efficiency (PCE) has been recently improved up to >13% with rapid advances in new photovoltaic materials [7]. In the typical bulk heterojunction (BHJ) OSCs configuration, a photoactive blend layer consisting of acceptor/donor pairs is sandwiched between a bottom transparent anode and a top low-work-function cathode, combined with the corresponding interlayers. Such interlayers are crucial for determining the overall PCE and stability of OSCs because they reduce the potential energy barrier between photoactive layer and electrodes, enhancing the extraction of holes and electrons at the anode and cathode, respectively.

Until now, many hole-transporting layer (HTL) materials, such as conducting conjugated polymers [8–10], conjugated polyelectrolytes [11,12] metal oxides/sulfides [13–17], and graphene oxide and its hybrid films [18–21], have been explored for use in OSCs. Among them, the conjugated polymer poly(3,4 ethylenedioxythiophene):poly(styrenesulfonate) (PEDOT:PSS) has been the most

widely used due to its adequate work function for creating a good ohmic contact between active layer and anode, solution processability, and high conductivity. However, its hygroscopic and acidic nature often induces chemical instability between active layers and indium tin oxide (ITO) anodes, affecting the device stability and efficiency [22,23]. Moreover, there is a clear surface energy mismatch between PEDOT:PSS (hydrophilic nature) and the active layer (hydrophobic and made of, e.g., poly(3-hexylthiophene) (P3HT)) [24,25]. To overcome such drawbacks, various PEDOT:PSS modification strategies, such as incorporating metal nanoparticles [26–28], modification by metal salts [29,30], polymer doping [31,32], and hybridization with graphene [33,34], have been developed. Interfacial engineering with long alkyl chains is an alternative but attractive method to reduce the surface energy mismatch between HTL and active layer and also to accomplish desirable molecular orientation in the active layer for enhancing the charge transport in OSCs [35].

Single and few-layer molybdenum disulfide, a two-dimensional (2D) transition metal dichalcogenide (TMDC), has recently received much interest in electronics and optoelectronics research due to its excellent optical (bandgap: 1.8 eV), electrical (device mobility: 10–130 cm^2 V^{-1} S^{-1}), and mechanical (Young modulus: 270 GPa) properties [36,37]. Among the key preparation/exfoliation methods for TMDCs, namely, micromechanical cleavage [38], chemical vapor deposition [39], and liquid-phase exfoliation (LPE) [40], the latter is more attractive because it is scalable and cost-effective. MoS_2 has been tested as HTL for OSCs [41–43] to exploit its extraordinary optical and electrical properties in photovoltaics; nevertheless, the results have revealed that neat MoS_2 is not sufficient to replace PEDOT:PSS as OSC HTL, possibly because of its work function mismatch and unexpected phase transition. Hence, Xing et al. fabricated PEDOT:PSS/WS_2 hybrid films and demonstrated their applicability as effective OSC HTLs [44]. However, the long-time (48 h) sonication they adopted for TMDC exfoliation in the PEDOT:PSS aqueous dispersion may affect the structure of both PEDOT:PSS and MoS_2 in the final product; therefore, innovative strategies for effectively integrating these materials in OSCs are still highly demanded.

Here, we report the fabrication of oleylamine-functionalized MoS_2 ($FMoS_2$) combined with PEDOT:PSS as an effective hybrid HTL (PEDOT:PSS/$FMoS_2$) for use in conventional P3HT:[6,6]-phenyl-C_{61}-butyric acid methyl ester (PCBM)-based OSCs. The so-obtained OSCs exhibited better PCE and short-circuit current density (J_{sc}) values compared with the reference cell having simple PEDOT:PSS as HTL. $FMoS_2$ was characterized by various spectroscopic techniques including Raman spectroscopy, ultraviolet–visible (UV-Vis) absorption and transmittance, photoluminescence (PL), and transmission electron microscopy (TEM); the active layer microstructure and the surface properties of the hybrid HTL were analyzed by grazing-incidence wide-angle X-ray scattering (GIWAXS), atomic force microscopy (AFM), and contact angle measurements. Electrochemical impedance spectroscopy (EIS) measurements were carried out using an electrochemical analyzer (IVIUMSTAT.XR, IVIUM Technologies) under illumination at 0.1 V.

2. Experimental

2.1. Materials and Methods

The following chemicals were used in our experiment: molybdenum (IV) sulfide (<2 μm, 99%) and oleylamine (Sigma-Aldrich, Gyeonggi-do, Korea), P3HT (1-Material, Gyeonggi-do, Korea), PEDOT:PSS (Heraeus Deutschland GmbH & Co., Leverkusen, Germany), isopropyl alcohol (IPA) (Dae-Jung Chemicals & Metals Co., Ltd., Gyeonggi-do, Korea), and methanol (Samchun Chemicals, Seoul, Korea).

2.2. Synthesis of $FMoS_2$ Nanosheets and PEDOT:PSS/$FMoS_2$ Hybrids

$FMoS_2$ nanosheets were synthesized according to the liquid-phase exfoliation method reported in literature [45], with small modifications. Briefly, bulk MoS_2 powder (200 mg) was bath-sonicated in oleylamine (2 mL) by using a Branson ultrasonic bath for 20 min and successively stirred at 60 °C for 12 h in an N_2-filled glove box. Then, 1,2-dichlorobenzene (DCB) (18 mL) was added, and the

dispersion was further bath-sonicated for 5 h. The resulting suspension was centrifuged at 4000 rpm, and the top 80% dark-green color supernatant, which contains excess oleylamine, DCB, and $FMOS_2$ was collected. Then, the $FMoS_2$ nanosheets were separated by adding excess acetone, followed by sonication for 2 min and high-speed centrifugation (10000 rpm). The separated $FMoS_2$ nanosheets were settled at the bottom of the centrifuge tube, which was re-dispersed in a small amount of IPA by mild sonication, and different concentrations (5, 20, and 50 µL) of the resulting dispersion were added into PEDOT:PSS:methanol (1:1 V%) aqueous solutions, which were successively ultrasonicated for 30 min to obtain PEDOT:PSS/$FMoS_2$ hybrid solutions.

2.3. Fabrication of OSCs

The OSCs having device architectures of ITO/PEDOT:PSS/P3HT:PCBM/LiF/Al and ITO/(PEDOT:PSS/$FMoS_2$)/P3HT:PCBM/LiF/Al were fabricated as follows. ITO-coated glass substrates were cleaned via sequential ultrasonication in acetone, IPA, and distilled water, followed by oxygen plasma treatment for 10 min; then, they were spin-coated with a PEDOT:PSS (Clevios P VP Al 4083) or PEDOT:PSS/$FMoS_2$ solution at 4000 rpm for 40 s and dried at 130 °C for 30 min to complete the HTL deposition. Next, an active layer consisting of a P3HT:PCBM (1:0.6 wt%) binary blend solution was spin-coated on the resulting HTL layer at 2500 rpm for 40 s inside an N_2-filled glove box and annealed at 150 °C. Finally, LiF and Al layers were deposited by thermal evaporation. The active area of the fabricated OSCs was 0.06 cm^2.

2.4. Characterization

The absorption properties of the samples were analyzed using a UV-Vis absorption spectrometer (Cary 5000, Varian, Inc.). Raman spectra were recorded on a Horiba Jobin-Yvon spectrometer. The emission properties were investigated with a luminescence spectrometer (LS55 Perkin Elmer). The TEM measurements were carried out on a JEOL JSM-2100-F system. The surface morphologies were investigated using a tapping-mode atomic force microscope (Veeco D3100). The water contact angles of the samples were measured with a KSV CAM 101 instrument. The GIWAXS analysis was conducted at the PLS-II 9A U-SAXs beamline of the Pohang Accelerator Laboratory (Korea) at the following operating conditions: incidence angle of ~0.12°, wavelength of 1.12 Å, and sample-to-detector distance of 224 nm. The GIWAXS patterns were recorded using a 2D charge-coupled device camera (Rayonix, SX-165, USA) with an exposure time of 10–30 s. The JV properties of the solar cells were measured with a Keithley 2400 solar cell IV measurement system under AM 1.5 G illumination at 100 mW cm^{-2}.

3. Results and Discussion

OSCs having two different device architectures, ITO/(PEDOT:PSS/$FMoS_2$)/P3HT:PCBM/LiF/Al and ITO/PEDOT:PSS/P3HT:PCBM/LiF/Al (for comparison), were fabricated as schematized in Figure 1.

First, we synthesized $FMoS_2$ nanosheets via the solution-phase ultrasonic exfoliation of bulk MoS_2 in the presence of oleylamine and 1,2-dichlorobenzene as a solvent; then, they were incorporated in different concentrations (5, 20, and 50 µL) into PEDOT:PSS, and the resulting PEDOT:PSS/$FMoS_2$ (denoted as PEDOT:PSS/$FMoS_2$(5), PEDOT:PSS/$FMoS_2$(20), and PEDOT:PSS/$FMoS_2$(50) according to the $FMoS_2$ loading) was used as HTL for conventional OSCs.

Raman spectroscopy is a powerful nondestructive technique for monitoring structural changes in 2D materials [46]. The Raman spectrum of bulk MoS_2 showed two characteristic peaks at 374.83 and 402.05 cm^{-1} corresponding, respectively, to the E^1_{2g} and A_{1g} vibrational modes (Figure 2a); the first arose from the in-plane vibration of Mo and S atoms, while the second resulted from the out-of-plane vibrations of sulfur [47,48]. As regards $FMoS_2$, the peaks for both the E^1_{2g} and A_{1g} vibrational modes were blue-shifted toward higher wavenumbers (respectively, 382.66 and 405.66 cm^{-1}), suggesting interactions between oleylamine and MoS_2. Moreover, the wavenumber difference between these two vibrational modes is closely related to the layer number present in the MoS_2 nanosheets [49], and in

our case, this difference decreased from 27.2 cm^{-1} for bulk MoS_2 to 23 cm^{-1} for $FMoS_2$ nanosheets, demonstrating the successful exfoliation of MoS_2 nanosheets during the oleylamine treatment.

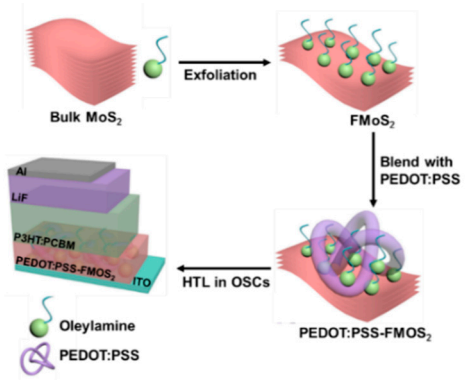

Figure 1. Fabrication process for poly(3,4-ethylenedioxythiophene):poly(styrenesulfonate) (PEDOT:PSS)/oleylamine-functionalized MoS_2 ($FMoS_2$) hybrid hole-transporting layer (HTL) for organic solar cells.

The absorption properties of the $FMoS_2$ nanosheets were further investigated via UV-Vis absorption spectroscopy; their spectrum (Figure 2b) clearly showed two characteristic absorption peaks of MoS_2 at 618 and 677 cm^{-1} corresponding, respectively, to the A1 and B1 direct excitonic transitions with the energy split from valence band spin–orbital coupling [50]. Furthermore, unlike bulk MoS_2, $FMoS_2$ yielded dark-greenish dispersion in 1,2-dichlorobenzene. These results clearly indicate some alteration in the surface properties of MoS_2 due to the oleylamine treatment [51].

Bulk MoS_2 is an indirect bandgap semiconductor that does not exhibit any photoluminescence; however, upon exfoliation, its luminescence increases with decreasing its layer thickness, so that single-layer MoS_2 shows the highest photoluminescence due to its transition into a direct bandgap semiconductor [52,53]. As expected, $FMoS_2$ exhibited significant photoluminescence (see the PL spectra in Figure S1, Electronic Supporting Information (ESI)), which clearly proves the successful layer thinning of MoS_2 during the functionalization process.

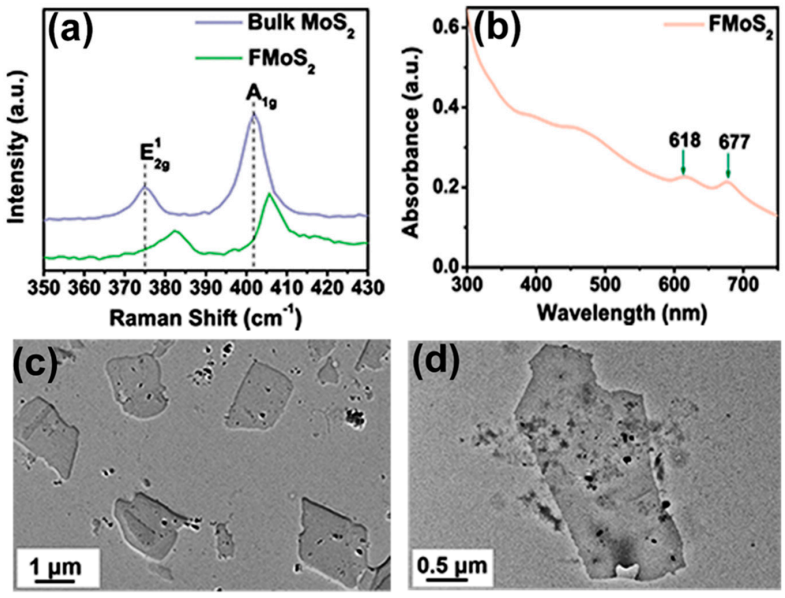

Figure 2. (**a**) Raman spectra of bulk and oleylamine-functionalized MoS_2 ($FMoS_2$). (**b**) Ultraviolet–visible light absorption spectrum of $FMoS_2$. (**c**,**d**) Transmission electron microscopy images of $FMoS_2$ nanosheets.

The TEM images of the $FMoS_2$ nanosheets are displayed in Figure 2c,d, showing a thin nanosheet morphology with sizes of several hundred nanometers. A careful observation of the nanosheet edges reveals the presence of few-layer nanosheets, confirming the effectiveness of the liquid-based exfoliation with oleylamine. AFM measurements were carried out (Figure S2, ESI) to further evaluate the layer thickness; that of $FMoS_2$ was ~6.7 nm, suggesting the existence of few-layer nanosheets, while the reported thickness of monolayer MoS_2 ranges between 0.9 and 1.2 nm [54].

To improve the performance of conventional PEDOT:PSS-based HTL for OSCs, we incorporated it with $FMoS_2$ via a simple solution-blending method because we believed that the introduction of 2D sheet-like MoS_2 functionalized with a long-chain primary alkyl amine (oleylamine) would have made the PEDOT:PSS surface more hydrophobic, facilitating the following deposition of the hydrophobic active layer. In addition, the amine group of oleylamine tends to be located near Mo atoms in MoS_2 due to metal–amine interactions, while its long alkyl chain with $–CH_3$ groups is oriented toward the active layer, and this kind of configuration should enforce the active layer with a desirable molecular orientation for efficient charge transport in OSCs; P3HT thin films deposited on insulator substrates modified with $–CH_3$ groups formed face-on orientation because of π–H interactions [55,56].

The contact angles of ITO with PEDOT:PSS and PEDOT:PSS/$FMoS_2$ containing 5, 20, and 50 μL of $FMoS_2$ were 30°, 47°, 54°, and 56°, respectively (Figure S3, ESI), which indicates that the hydrophobicity of PEDOT:PSS was slightly increased by the $FMoS_2$ addition and, hence, the hydrophobic active layer solution was more compatible on hybrid HTL than that of the hydrophilic PEDOT:PSS one.

The surface morphology of the various samples was compared via tapping-mode AFM analysis (Figure S4, ESI); the root-mean-square (rms) roughness value of PEDOT:PSS was 1 nm and decreased down to 0.69 nm for PEDOT:PSS/$FMoS_2$(5), suggesting a smooth surface morphology in the hybrid HTL. However, PEDOT:PSS/$FMoS_2$(50) exhibited an rms roughness value of 0.97 nm, indicating that the addition of higher $FMoS_2$ concentrations would decrease the film smoothness.

All the synthesized PEDOT:PSS and PEDOT:PSS/$FMoS_2$ hybrid films exhibited similar UV-Vis transmittance values (Figure S5a, ESI), showing that the $FMoS_2$ addition did not affect any absorption property of the PEDOT:PSS matrix. As regards the P3HT:PCBM (active layer) films spin-coated on glass substrates predeposited with PEDOT:PSS or PEDOT:PSS/$FMoS_2$ HTLs (Figure S5b), for all the samples, their absorbance ranged from 400 to 650 nm, with a maximum at 512 nm, and two shoulders around 550 and 600 nm. The existence of vibronic feature at 600 nm suggests that the P3HT film existed in a high degree of ordered crystalline lamella due to strong interchain interactions [57].

The current–voltage (JV) characteristics of the fabricated P3HT:PCBM OSCs having PEDOT:PSS/$FMoS_2$ as HTL are shown in Figure 3a. Their performance is compared with that of reference devices having PEDOT:PSS as HTL in Table 1. The reference cells showed PCE = 3.25%, J_{sc} = 7.92 mA cm^{-2}, V_{oc} = 0.671 V, and FF = 0.61. The $FMoS_2$ incorporation led to significant PCE and J_{sc} improvements; in particular, the device based on PEDOT:PSS/$FMoS_2$(5) exhibited the highest PCE, J_{sc}, and FF.

The external quantum efficiency (EQE) measurements (Figure 3b) showed improved EQE for the hybrid HTL-based OSCs compared with the reference cells and confirmed also their increased J_{sc}, demonstrating the enhanced charge extraction at the HTL/active layer interface and the charge collection at the electrodes [58,59]. The photovoltaic parameters such as PCE, J_{sc}, FF and V_{oc} as a function of $FMoS_2$ in PEDOT:PSS HTLs are plotted in Figure 3c, d, e and f respectively.

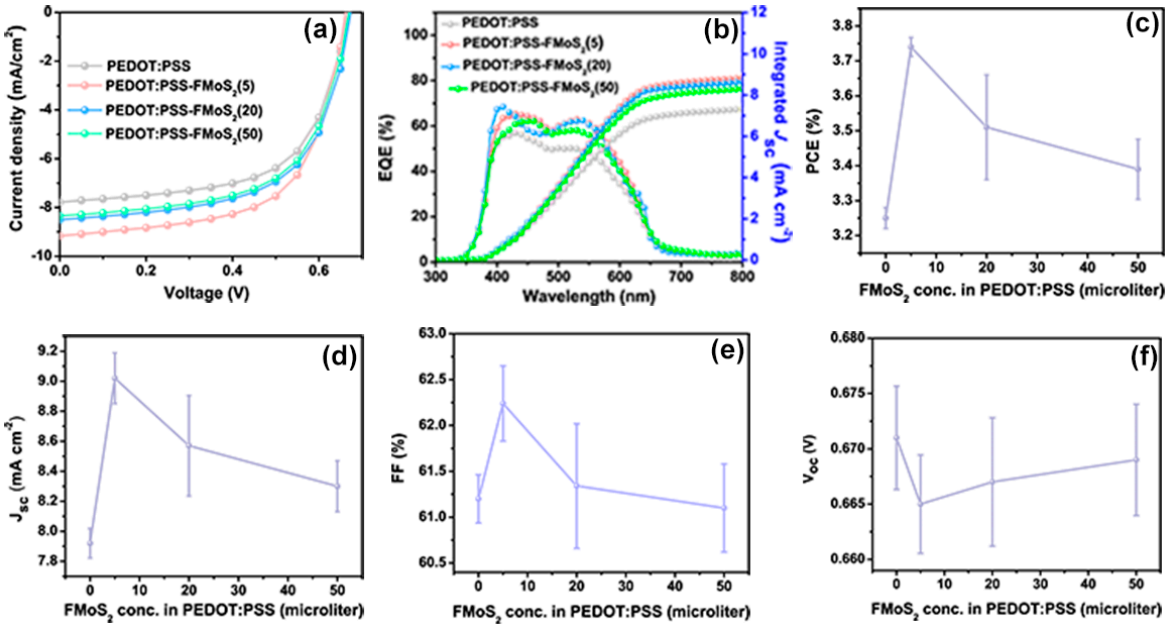

Figure 3. (**a**) Current density–voltage curves, (**b**) external quantum efficiency (EQE) profiles, (**c**) power conversion efficiencies (PCE), (**d**) short-circuit current density (J_{sc}), (**e**) fill factor, and (**f**) open-circuit voltage (V_{oc}) values of organic solar cells based on poly(3,4-ethylenedioxythiophene):poly(styrenesulfonate) (PEDOT:PSS) and PEDOT:PSS/oleylamine-functionalized MoS_2 ($FMoS_2$) as hole-transporting layers. The reported average PCE values are extracted from nine identical cells for each sample.

Table 1. Photovoltaic performance of poly(3-hexylthiophene):[6,6]-phenyl-C61-butyric acid methyl ester-based organic solar cells having poly(3,4-ethylenedioxythiophene):poly(styrenesulfonate) (PEDOT:PSSS) and PEDOT:PSS/oleylamine-functionalized MoS_2 ($FMoS_2$) as hole-transportation layers.

$FMoS_2$ Concentration (μL) in PEDOT:PSS	PCE (%)	V_{oc} (V)	J_{sc} (mA cm^{-2})	FF (%)
0 (Reference)	3.25 ± 0.03	0.671 ± 0.004	7.92 ± 0.09	61.2 ± 0.26
5	3.74 ± 0.02	0.665 ± 0.004	9.02 ± 0.17	62.24 ± 0.41
20	3.51 ± 0.15	0.667 ± 0.006	8.57 ± 0.33	61.34 ± 0.68
50	3.39 ± 0.08	0.669 ± 0.005	8.30 ± 0.17	61.10 ± 0.48

To understand the charge transport, we analyzed the microstructure (chain-orientation and crystallinity) of the active layer (P3HT:PCBM) on both the PEDOT:PSS and PEDOT:PSS/$FMoS_2$ samples by GIWAXS (Figures 4 and 5). Charge transport in conjugated polymers occurs either in the π–π staking direction or the chain backbone one, which is the fastest but its vertical alignment of chains backbones along the z direction is rarely observed [60,61]. In general, P3HT crystallizes into two main configurations, namely, edge-on and face-on orientations; in the former, both chain backbone and π–π staking directions lie parallel to the substrate; in the latter, π–π staking occurs perpendicular to the substrate, which is a desirable orientation in OSCs for vertical charge transport [62]. Figure 4 shows the GIWAXS diffraction patterns of P3HT:PCBM thin films deposited on PEDOT:PSS and PEDOT:PSS/$FMoS_2$ HTLs. In both cases, the thin films exhibited strong (100), (200), and (300) diffractions along the z axis, confirming the existence of the strong edge-on lamellae configuration of P3HT [63]. In addition, the absence of π–π staking peak (010), corresponding to the face-on orientation near the z axis, indicates that P3HT preferentially adopted the edge-on configuration in both PEDOT:PSS and PEDOT:PSS/$FMoS_2$ HTLs. Since the use of $–CH_3$ group-functionalized substrates tends to promote the face-on orientation of P3HT [55,56], we aimed to improve such configuration of the active layer by incorporating the described oleylamine (having $–CH_3$ groups)-functionalized

MoS_2 into PEDOT:PSS, but we did not observe any significant difference in its molecular orientation, maybe because the low $FMoS_2$ concentrations used were not sufficient for such change. Thus, we can conclude that the PCE and J_{sc} enhancement in the OCSs having PEDOT:PSS/$FMoS_2$ as HTL may be due to its surface compatibility for the active layer deposition, as observed in the AFM and contact angle measurements.

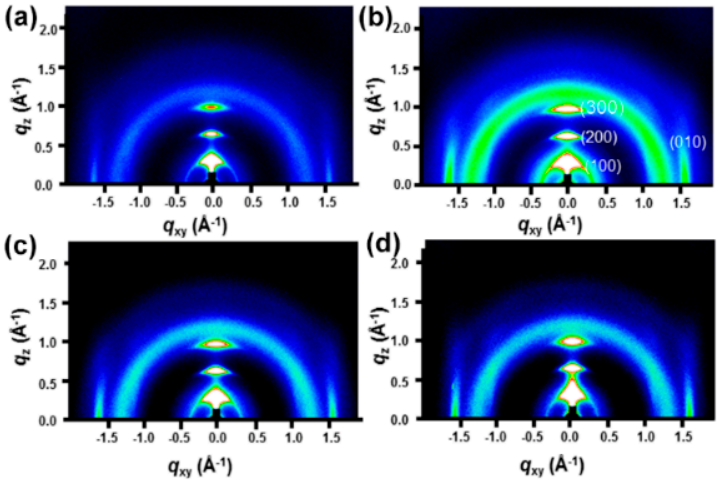

Figure 4. Grazing-incidence wide-angle X-ray scattering diffraction patterns of poly(3-hexylthiophene):[6,6]-phenyl-C_{61}-butyric acid methyl ester thin films deposited on (**a**) poly(3,4-ethylenedioxythiophene):poly(styrenesulfonate) (PEDOT:PSS) and PEDOT:PSS combined with (**b**) 5, (**c**) 20, and (**d**) 50 µL of oleylamine-functionalized MoS_2.

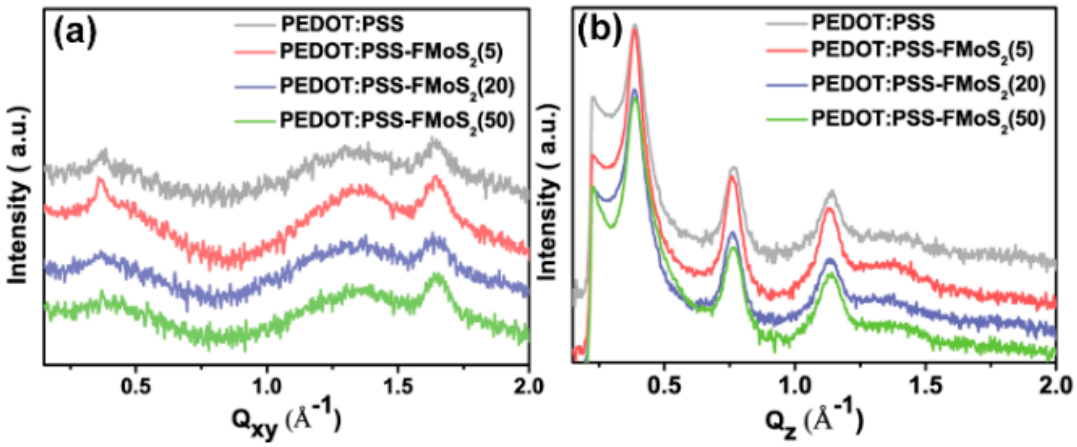

Figure 5. (**a**) In-plane and (**b**) out-of-plane spectra of poly(3-hexylthiophene):[6,6]-phenyl-C61-butyric acid methyl ester thin films deposited on poly (3,4-ethylendioxythiophene): poly(styrenesulfonate) (PEDOT:PSS) and PEDOT:PSS combined with 5, 20, and 50 µL of oleylamine-functionalized MoS_2 samples obtained from grazing-incidence wide-angle X-ray scattering.

Electrical impedance spectroscopy (EIS) was performed to investigate the charge transport dynamics of the OSCs fabricated with PEDOT:PSS and PEDOT:PSS/$FMoS_2$(5) as HTL (Figure 6). This analysis allowed us to observe the current response by applying alternating current voltage as a function of frequency; the OSCs with PEDOT:PSS/$FMoS_2$(5) demonstrated slightly lower charge transfer resistance, revealing that the holes were effectively transported from the active layer to the anode (ITO). In order to elucidate the origin of the improvement in the photovoltaic performance, especially both FF and J_{sc} for PEDOT:PSS/$FMoS_2$(5), we further calculated the resistance of the devices. In general, it is well known that lower series resistance (R_S) and higher shunt resistance (R_{SH}) are required to achieve higher FF in the solar cell device [64]. Based on the J–V curves obtained from the

devices, it is clearly revealed that the device with PEDOT:PSS/$FMoS_2$(5) as HTL showed the lowest R_S while maintaining higher R_{SH}, leading to enhancement in charge extraction. The corresponding R_S value of cells employing PEDOT:PSS/$FMoS_2$(5) as HTL was 134.8 $\Omega \cdot cm^2$, while the reference showed 180.0 $\Omega \cdot cm^2$. Lower R_S indicates that better interfacial contact and charge collection efficiency were obtained due to the addition of the conducting $FMoS_2$ layer. In the case of the R_{SH}, no significant changes in the shunt resistance were observed for the devices. In the point of view of the identical R_{SH}, barrier resistance at the interface and the leakage current level flowing across the photoactive layer is similar. Therefore, the addition of $FMoS_2$ might contribute to extract photoexcited charges efficiently by lowering the R_S.

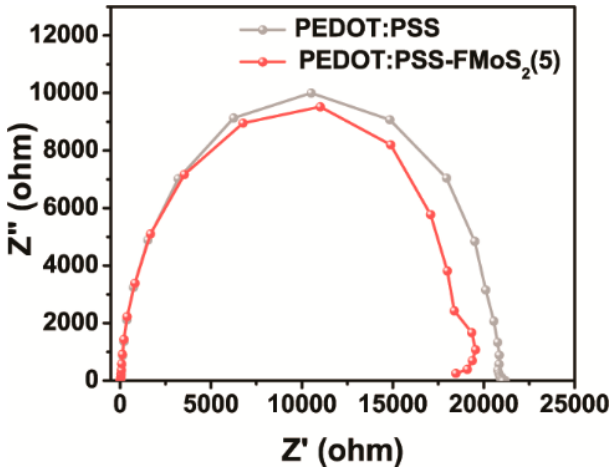

Figure 6. Electrical impedance spectra of organic solar cells based on poly(3,4-ethylenedioxythiophene):poly(styrenesulfonate) (PEDOT:PSS) and PEDOT:PSS/oleylamine-functionalized MoS_2 (5 μL) (PEDOT:PSS/$FMoS_2$(5)) as hole-transportation layer.

4. Conclusions

The application of solution-processed PEDOT:PSS/$FMoS_2$ hybrids as effective HTLs for OSCs has been successfully demonstrated. Raman, UV-Vis, PL, TEM, and AFM analyses confirmed the successful exfoliation of bulk MoS_2 into few-layer nanosheets in the presence of oleylamine via a simple and cost-effective solution-based method. The OSCs fabricated with the synthesized PEDOT:PSS/$FMoS_2$ hybrids as HTL exhibited PCE values up to 3.74%, which is 15.08% higher than that of the reference cells having simple PEDOT:PSS as HTL. The hybrid HTL films showed better surface properties for the deposition of the hydrophobic active layer, consequently, the charge-transfer resistance was minimized for OSCs fabricated with hybrid HTL compared with reference cells, improving the OSC performance. Due to their simple preparation method, 2D $FMoS_2$-incorporated PEDOT:PSS-based HTL provides valuable alternative HTL for OSCs.

Supplementary Materials: The following are available online at http://www.mdpi.com/2079-4991/9/9/1328/s1, Figures S1 and S2: PL spectra and AFM image of oleylamine-functionalized MoS_2 ($FMoS_2$) respectively, Figures S3 and S4: Contact angles and AFM images of PEDOT:PSS and PEDOT:PSS combined with $FMoS_2$ respectively, Figure S5: (a) UV-Vis transmittance spectra of PEDOT:PSS and PEDOT:PSS combined with $FMoS_2$, (b) UV-Vis absorbance spectra of P3HT:PCBM thin film spin-coated on PEDOT:PSS and PEDOT:PSS $FMoS_2$.

Author Contributions: M.S.R., prepared the content of this research, carried out device fabrication, analysis of results and wrote the manuscript. K.Y.R. performed GIWAXS measurements and interpreted the data. J.W.L. performed IPCE measurements and guided for manuscript revisions. A.B., H.K., J.-E.L. performed the design of device configuration, performed AFM and PL measurements. D.H.K. and K.K. guided the overall scope of this research and wrote the manuscript.

Funding: This work was supported by National Research Foundation of Korea Grant funded by the Korean Government (2017R1A2A1A05022387 and 2016M1A2A2940914) and by the Korea Institute of Energy Technology Evaluation and Planning (KETEP) and the Ministry of Trade, Industry & Energy (MOTIE) of the Republic of Korea (No. 20173010013340 and 20163030013900).

Conflicts of Interest: There are no conflicts to declare.

References

1. Jang, Y.H.; Jang, Y.J.; Kim, S.; Quan, L.N.; Chung, K.; Kim, D.H. Plasmonic solar cells: From rational design to mechanism overview. *Chem. Rev.* **2016**, *116*, 14982–15034. [CrossRef] [PubMed]
2. Oh, Y.; Lim, J.W.; Kim, J.G.; Wang, H.; Kang, B.H.; Park, Y.W.; Kim, H.; Jang, Y.J.; Kim, J.; Kim, D.H.; et al. Plasmonic periodic nanodot arrays via laser interference lithography for organic photovoltaic cells with >10% efficiency. *ACS Nano* **2016**, *10*, 10143–10151. [CrossRef] [PubMed]
3. Xie, L.; Lee, J.S.; Jang, Y.; Ahn, H.; Kim, Y.H.; Kim, K. Organic photovoltaics utilizing a polymer nanofiber/fullerene interdigitated bilayer prepared by sequential solution deposition. *J. Phys. Chem. C* **2016**, *120*, 12933–12940. [CrossRef]
4. Zhu, M.; Kim, H.; Jang, Y.J.; Park, S.; Ryu, D.Y.; Kim, K.; Tang, P.; Qiu, F.; Kim, D.H.; Peng, J. Toward high efficiency organic photovoltaic devices with enhanced thermal stability utilizing P3HT-b-P3PHT block copolymer additives. *J. Mater. Chem. A* **2016**, *4*, 18432–18443. [CrossRef]
5. Kim, Y.; Son, J.; Shafian, S.; Kim, K.; Hyun, J.K. Semitransparent blue, green, and red organic solar cells Using Color Filtering Electrodes. *Adv. Opt. Mater.* **2018**, *6*, 1800051. [CrossRef]
6. Xie, L.; Yoon, S.; Cho, Y.J.; Kim, K. Effective protection of sequential solution-processed polymer/fullerene bilayer solar cell against charge recombination and degradation. *Org. Electron.* **2015**, *25*, 212–218. [CrossRef]
7. Zhao, W.; Li, S.; Yao, H.; Zhang, S.; Zhang, Y.; Yang, B.; Hou, J. Molecular optimization enables over 13% efficiency in organic solar cells. *J. Am. Chem. Soc.* **2017**, *139*, 7148–7151. [CrossRef] [PubMed]
8. Ahn, S.; Jeong, S.H.; Han, T.H.; Lee, T.W. Conducting polymers as anode buffer materials in organic and perovskite optoelectronics. *Adv. Opt. Mater.* **2017**, *5*, 1600512. [CrossRef]
9. Zhang, S.; Yu, Z.; Li, P.; Li, B.; Isikgor, F.H.; Du, D.; Sun, K.; Xia, Y.; Ouyang, J. Poly(3,4-ethylenedioxythiophene): Polystyrene sulfonate films with low conductivity and low Acidity through a treatment of their solutions with probe ultrasonication and their application as hole transport layer in polymer solar cells and perovskite solar cells. *Org. Electron.* **2016**, *32*, 149–156.
10. Lee, J.J.; Lee, S.H.; Kim, F.S.; Choi, H.H.; Kim, J.H. Simultaneous enhancement of the efficiency and stability of organic solar cells using PEDOT: PSS grafted with a PEGME buffer layer. *Org. Electron.* **2015**, *26*, 191–199. [CrossRef]
11. Zhou, H.; Zhang, Y.; Mai, C.K.; Seifter, J.; Nguyen, T.Q.; Bazan, G.C.; Heeger, A.J. Solution-processed pH-neutral conjugated polyelectrolyte improves interfacial contact in organic solar cells. *ACS Nano* **2015**, *9*, 371–377. [CrossRef] [PubMed]
12. Zhou, H.; Zhang, Y.; Mai, C.K.; Collins, S.D.; Nguyen, T.Q.; Bazan, G.C.; Heeger, A.J. Conductive conjugated polyelectrolyte as hole-transporting layer for organic bulk heterojunction solar cells. *Adv. Mater.* **2014**, *26*, 780–785. [CrossRef] [PubMed]
13. Jasieniak, J.J.; Seifter, J.; Jo, J.; Mates, T.; Heeger, A.J. A solution-processed MoOx anode interlayer for use within organic photovoltaic devices. *Adv. Funct. Mater.* **2012**, *22*, 2594–2605. [CrossRef]
14. Xie, F.; Choy, W.C.H.; Wang, C.; Li, X.; Zhang, S.; Hou, J. Low-temperature solution-processed hydrogen molybdenum and vanadium bronzes for an efficient hole-transport layer in organic electronics. *Adv. Mater.* **2013**, *25*, 2051–2055. [CrossRef] [PubMed]
15. Bao, X.; Zhu, Q.; Wang, T.; Guo, J.; Yang, C.; Yu, D.; Wang, N.; Chen, W.; Yang, R. Simple O_2 plasma-processed V_2O_5 as an anode buffer layer for high performance polymer solar cells. *ACS Appl. Mater. Interfaces* **2015**, *7*, 7613–7618. [CrossRef] [PubMed]
16. Bai, S.; Jin, Y.; Dai, X.; Liang, X.; Ye, Z.; Li, M.; Cheng, J.; Xiao, X.; Wu, Z.; Xia, Z.; et al. Low-temperature combustion-synthesized nickel oxide thin films as hole-transport interlayers for solution processed optoelectronic devices. *Adv. Energy Mater.* **2014**, *4*, 1301460. [CrossRef]
17. Yin, Z.; Wei, J.; Zheng, Q. Interfacial materials for organic solar cells: Recent advances and perspectives. *Adv. Sci.* **2016**, *3*, 1500362. [CrossRef] [PubMed]
18. Liu, J.; Xue, Y.; Dai, L. Sulfated graphene oxide as a hole-extraction layer in high-performance polymer solar cells. *J. Phys. Chem. Lett.* **2012**, *3*, 1928–1933. [CrossRef]
19. Li, S.S.; Tu, K.H.; Lin, C.C.; Chen, C.W.; Chhowalla, M. Solution-processable graphene oxide as an efficient hole transport layer in polymer solar cells. *ACS Nano* **2010**, *4*, 3169–3174. [CrossRef]

20. Yun, J.M.; Yeo, J.S.; Kim, J.; Jeong, H.G.; Kim, D.Y.; Noh, Y.J.; Kim, S.S.; Ku, B.C.; Na, S.I. Solution-processable reduced graphene oxide as a novel alternative to PEDOT:PSS hole transport layers for highly efficient and stable polymer solar cells. *Adv. Mater.* **2011**, *23*, 4923–4928. [CrossRef]
21. Niu, J.; Yang, D.; Ren, X.; Yang, Z.; Liu, Y.; Zhu, X.; Zhao, W.; Liu, S. Graphene-oxide doped PEDOT: PSS as a superior hole transport material for high-efficiency perovskite solar cell. *Org. Electron.* **2017**, *48*, 165–171. [CrossRef]
22. Drakonakis, V.M.; Savva, A.; Kokonou, M.; Choulis, S.A. Investigating electrodes degradation in organic photovoltaics through reverse engineering under accelerated humidity lifetime conditions. *Sol. Energy Mater. Sol. Cells* **2014**, *130*, 544–550. [CrossRef]
23. Kawano, K.; Pacios, R.; Poplavskyy, D.; Nelson, J.; Bradley, D.D.C.; Durrant, J.R. Degradation of organic solar cells due to air exposure. *Sol. Energy Mater. Sol. Cells* **2006**, *90*, 3520–3530. [CrossRef]
24. Lim, F.J.; Ananthanarayanan, K.; Luther, J.; Ho, G.W. Influence of a novel fluorosurfactant modified PEDOT: PSS hole transport layer on the performance of inverted organic solar cells. *J. Mater. Chem.* **2012**, *22*, 25057–25064. [CrossRef]
25. Arulkashmir, A.; Krishnamoorthy, K. Disassembly of micelles to impart donor and acceptor gradation to enhance organic solar cell efficiency. *Chem. Commun.* **2016**, *52*, 3486–3489. [CrossRef]
26. Lim, D.C.; Kim, K.D.; Park, S.Y.; Hong, E.M.; Seo, H.O.; Lim, J.H.; Lee, K.W.; Jeong, Y.J.; Song, C.; Lee, E.; et al. Towards fabrication of high-performing organic photovoltaics: New donor polymer, atomic layer deposited thin buffer layer and plasmonic effects. *Energy Environ. Sci.* **2012**, *5*, 9803–9807. [CrossRef]
27. Wang, K.; Yi, C.; Hu, X.; Liu, C.; Sun, Y.; Hou, J.; Li, Y.; Zheng, J.; Chuang, S.; Karim, A.; et al. Enhanced performance of polymer solar cells using PEDOT:PSS doped with Fe_3O_4 magnetic nanoparticles aligned by an external magnetostatic field as an anode buffer layer. *ACS Appl. Mater. Interfaces* **2014**, *6*, 13201–13208. [CrossRef]
28. Yao, K.; Salvador, M.; Chueh, C.C.; Xin, X.K.; Xu, Y.X.; de Quilettes, D.W.; Hu, T.; Chen, Y.; Ginger, D.S.; Jen, A.K.Y. A general route to enhance polymer solar cell performance using plasmonic nanoprisms. *Adv. Energy Mater.* **2014**, *4*, 1400206. [CrossRef]
29. Zhao, Z.; Wu, Q.; Xia, F.; Chen, X.; Liu, Y.; Zhang, W.; Zhu, J.; Dai, S.; Yang, S. Improving the conductivity of PEDOT: PSS hole transport layer in polymer solar cells via copper(II) bromide salt doping. *ACS Appl. Mater. Interfaces* **2015**, *7*, 1439–1448. [CrossRef]
30. Kadem, B.; Cranton, W.; Hassan, A. Metal salt modified PEDOT: PSS as anode buffer layer and its effect on power conversion efficiency of organic solar cells. *Org. Electron.* **2015**, *24*, 73–79. [CrossRef]
31. Kang, D.J.; Cho, H.H.; Lee, I.; Kim, K.H.; Kim, H.J.; Liao, K.; Kim, T.S.; Kim, B.J. Enhancing mechanical properties of highly efficient polymer solar cells using size-tuned polymer nanoparticles. *ACS Appl. Mater. Interfaces* **2015**, *7*, 2668–2676. [CrossRef]
32. Hossain, J.; Liu, Q.; Miura, T.; Kasahara, K.; Harada, D.; Ishikawa, R.; Ueno, K.; Shirai, H. Nafion-modified PEDOT: PSS as a transparent hole-transporting layer for high-performance crystalline-Si/organic heterojunction solar cells with improved light soaking stability. *ACS Appl. Mater. Interfaces* **2016**, *8*, 31926–31934. [CrossRef]
33. Hilal, M.; Han, J.I. Significant improvement in the photovoltaic stability of bulk heterojunction organic solar cells by the molecular level interaction of graphene oxide with a PEDOT: PSS composite hole transport layer. *Sol. Energy* **2018**, *167*, 24–34. [CrossRef]
34. HDehsari, S.; Shalamzari, E.K.; Gavgani, J.N.; Taeomi, F.A.; Ghanbary, S. Efficient preparation of ultralarge graphene oxide using a PEDOT: PSS/GO composite layer as hole transport layer in polymer-based optoelectronic devices. *RSC Adv.* **2014**, *4*, 55067–55076. [CrossRef]
35. Walker, B.; Choi, H.; Kim, J.Y. Interfacial engineering for highly efficient organic solar cells. *Curr. Appl. Phys.* **2017**, *17*, 370–391. [CrossRef]
36. Pham, V.P.; Yeom, G.Y. Recent advances in doping of molybdenum disulfide: Industrial applications and future prospects. *Adv. Mater.* **2016**, *28*, 9024–9059. [CrossRef]
37. Chhowalla, M.; Shin, H.S.; Eda, G.; Li, L.J.; Loh, K.P.; Zhang, H. The chemistry of two-dimensional layered transition metal dichalcogenide nanosheets. *Nat. Chem.* **2013**, *5*, 263–275. [CrossRef]
38. Li, H.; Wu, J.; Yin, Z.; Zhang, H. Preparation and Applications of Mechanically Exfoliated Single-Layer and Multilayer MoS_2 and WSe_2 Nanosheets. *Acc. Chem. Res.* **2014**, *47*, 1067–1075. [CrossRef]

39. Lee, Y.H.; Zhang, X.Q.; Zhang, W.; Chang, M.T.; Lin, C.T.; Chang, K.D.; Yu, Y.C.; Wang, J.T.W.; Chang, C.S.; Li, L.J.; et al. Synthesis of large-area MoS_2 atomic layers with chemical vapor deposition. *Adv. Mater.* **2012**, *24*, 2320–2325. [CrossRef]
40. Zhang, X.; Lai, Z.; Tan, C.; Zhang, H. Solution-processed two-Dimensional MoS_2 nanosheets: Preparation, hybridization, and applications. *Angew. Chem. Int. Ed.* **2016**, *55*, 8816–8838. [CrossRef]
41. Le, Q.V.; Nguyen, T.P.; Jang, H.W.; Kim, S.Y. The use of UV/ozone-treated MoS_2 nanosheets for extended air stability in organic photovoltaic cells. *Phys. Chem. Chem. Phys.* **2014**, *16*, 13123–13128. [CrossRef]
42. Yun, J.M.; Noh, Y.J.; Yeo, J.S.; Go, Y.J.; Na, S.I.; Jeong, H.G.; Kim, J.; Lee, S.; Kim, S.S.; Koo, H.Y.; et al. Efficient work-function engineering of solution-processed MoS_2 thin-films for novel hole and electron transport layers leading to high-performance solar cells. *J. Mater. Chem. C* **2013**, *1*, 3777–3783. [CrossRef]
43. Yang, X.; Fu, W.; Liu, W.; Hong, J.; Cai, Y.; Jin, C.; Xu, M.; Wang, H.; Yang, D.; Chen, H. Engineering crystalline structures of two-dimensional MoS_2 sheets for high-performance organic solar cells. *J. Mater. Chem. A* **2014**, *2*, 7727–7733. [CrossRef]
44. Xing, W.; Chen, Y.; Wu, X.; Xu, X.; Ye, P.; Zhu, T.; Guo, Q.; Yang, L.; Li, W.; Huang, H. PEDOT: PSS-assisted exfoliation and functionalization of 2D nanosheets for high-performance organic solar cells. *Adv. Funct. Mater.* **2017**, *27*, 1701622. [CrossRef]
45. Ahmad, R.; Srivastava, R.; Yadav, S.; Chand, S.; Sapra, S. Functionalized 2D-MoS_2-incorporated polymer ternary solar cells: Role of nanosheet-induced long-range ordering of polymer chains on charge transport. *ACS Appl. Mater. Interfaces* **2017**, *9*, 34111–34121. [CrossRef]
46. Wu, J.B.; Lin, M.L.; Cong, X.; Liu, H.N.; Tan, P.H. Raman spectroscopy of graphene-based materials and its applications in related devices. *Chem. Soc. Rev.* **2018**, *47*, 1822–1873. [CrossRef]
47. Cho, K.; Min, M.; Kim, T.Y.; Jeong, H.; Pak, J.; Kim, J.K.; Jang, J.; Yun, S.J.; Lee, Y.H.; Hong, W.K.; et al. Electrical and optical characterization of MoS_2 with Sulfur vacancy passivation by treatment with alkanethiol molecules. *ACS Nano* **2015**, *9*, 8044–8053. [CrossRef]
48. Yao, Y.; Tolentino, L.; Yang, Z.; Song, X.; Zhang, W.; Chen, Y.; Wong, C. High-concentration aqueous dispersions of MoS_2. *Adv. Funct. Mater.* **2013**, *23*, 3577–3583. [CrossRef]
49. Luo, S.; Qi, X.; Ren, L.; Hao, G.; Fan, Y.; Liu, Y.; Han, W.; Zang, C.; Li, J.; Zhong, J. Photoresponse properties of large-area MoS_2 atomic layer synthesized by vapor phase deposition. *J. Appl. Phys.* **2014**, *116*, 164304. [CrossRef]
50. Zhou, K.G.; Mao, N.N.; Wang, H.X.; Peng, Y.; Zhang, H.L. A Mixed-solvent strategy for efficient exfoliation of inorganic graphene analogues. *Angew. Chem. Int. Ed.* **2011**, *50*, 10839–10842. [CrossRef]
51. Chen, X.; Berner, N.C.; Backes, C.; Duesberg, G.S.; McDonald, A.R. Functionalization of two-dimensional MoS_2: On the reaction between MoS_2 and organic thiols. *Angew. Chem. Int. Ed.* **2016**, *55*, 5803–5808. [CrossRef]
52. Splendiani, A.; Sun, L.; Zhang, Y.; Li, T.; Kim, J.; Chim, C.Y.; Galli, G.; Wang, F. Emerging photoluminescence in monolayer MoS_2. *Nano Lett.* **2010**, *10*, 1271–1275. [CrossRef]
53. Eda, G.; Yamaguchi, H.; Voiry, D.; Fujita, T.; Chen, M.; Chhowalla, M. Photoluminescence from chemically exfoliated MoS_2. *Nano. Lett.* **2011**, *11*, 5111–5116. [CrossRef]
54. Qi, Y.; Wang, N.; Xu, Q.; Li, H.; Zhou, P.; Lu, X.; Zhao, G. A green route to fabricate MoS_2 nanosheets in water-ethanol-CO_2. *Chem. Commun.* **2015**, *51*, 6726–6729. [CrossRef]
55. Kim, D.H.; Park, Y.D.; Jang, Y.; Yang, H.; Kim, Y.H.; Han, J.I.; Moon, D.G.; Park, S.; Chang, T.; Chang, C.; et al. Enhancement of field-effect mobility due to surface-mediated molecular ordering in regioregular polythiophene thin film transistors. *Adv. Funct. Mater.* **2005**, *15*, 77–82. [CrossRef]
56. Kim, D.H.; Jang, Y.; Park, Y.D.; Cho, K. Surface-induced conformational changes in poly(3-hexylthiophene) monolayer films. *Langmuir* **2005**, *21*, 3203–3206. [CrossRef]
57. Huang, J.S.; Goh, T.; Li, X.; Sfeir, M.Y.; Bielinski, E.A.; Tomasulo, S.; Lee, M.L.; Hazari, N.; Taylor, A.D. Polymer bulk heterojunction solar cells employing Forster resonance energy transfer. *Nat. Photonics* **2013**, *7*, 479–485. [CrossRef]
58. Liu, Y.; Renna, L.A.; Page, Z.A.; Thompson, H.B.; Kim, P.Y.; Barnes, M.D.; Emrick, T.; Venkataramanan, D.; Russell, T.P. A polymer hole extraction layer for inverted perovskite solar cells from aqueous solutions. *Adv. Energy Mater.* **2016**, *6*, 1600664. [CrossRef]

59. Choi, H.; Kim, H.B.; Ko, S.J.; Kim, J.Y.; Heeger, A.J. An organic surface modifier to produce a high work function transparent electrode for high performance polymer solar cells. *Adv. Mater.* **2015**, *27*, 892–896. [CrossRef]
60. Noriega, R.; Rivnay, J.; Vandewal, K.; Koch, F.P.V.; Stingelin, N.; Smith, P.; Toney, M.F.; Salleo, A. A general relationship between disorder, aggregation and charge transport in conjugated polymers. *Nat. Mater.* **2013**, *12*, 1038–1044. [CrossRef]
61. Lan, Y.K.; Huang, C. A theoretical study of the charge transfer behavior of the highly regioregular poly-3-hexylthiophene in the ordered state. *J. Phys. Chem. B* **2008**, *112*, 14857–14862. [CrossRef]
62. Skrypnychuk, V.; Boulanger, N.; Yu, V.; Hilke, M.; Mannsfeld, S.C.B.; Toney, M.F.; Barbero, D.R. Enhanced vertical charge transport in a semiconducting P3HT thin Film on single layer grapheme. *Adv. Funct. Mater.* **2015**, *25*, 664–670. [CrossRef]
63. Boulanger, N.; Yu, V.; Hilke, M.; Toney, M.F.; Barbero, D.R. In situ probing of the crystallization kinetics of rr-P3HT on single layer graphene as a function of temperature. *Phys. Chem. Chem. Phys.* **2017**, *19*, 8496–8503. [CrossRef]
64. Lim, J.W.; Wang, H.; Choi, C.H.; Quan, L.N.; Chung, K.; Park, W.T.; Noh, Y.Y.; Kim, D.H. Polyethylenimine ethoxylated interlayer-mediated ZnO interfacial engineering for high-performance and low-temperature processed flexible perovskite solar cells: A simple and viable route for one-step processed $CH_3NH_3PbI_3$. *J. Power Sources* **2019**, *438*, 226956. [CrossRef]